

Article

Three-Dimensional Probe Mispositioning Errors Compensation: A Feasibility Study in the Non-Redundant Helicoidal Near to Far-Field Transformation Case

Francesco D'Agostino ¹, Flaminio Ferrara ¹, Claudio Gennarelli ¹, Rocco Guerriero ^{1,*}, Massimo Migliozi ¹, Luigi Pascarella ¹ and Giovanni Riccio ²

¹ Department of Industrial Engineering, University of Salerno, Via Giovanni Paolo II, 84084 Fisciano, Salerno, Italy; fdagostino@unisa.it (F.D.); flferrara@unisa.it (F.F.); cgennarelli@unisa.it (C.G.); mmigliozi@unisa.it (M.M.); lpascarella@unisa.it (L.P.)

² Department of Information and Electrical Engineering and Applied Mathematics, University of Salerno, Via Giovanni Paolo II, 84084 Fisciano, Salerno, Italy; griccio@unisa.it

* Correspondence: rguerriero@unisa.it; Tel.: +39-08-996-4259

Abstract: A feasibility study on the compensation of 3D mispositioning errors of the probe occurring in the characterization of a long antenna, via a non-redundant (NR) near to far-field (NTFF) transformation with helicoidal scan, is conducted in this article. Such types of errors can result from imperfections in the rail driving the linear motion of the probe and from an imprecise synchronization of the linear and rotational movements of the probe and the antenna when drawing the scan helix. To correct them, an approach, which proceeds through two steps, is proposed. The former step uses a technique called cylindrical wave (CW) correction for compensating the phase of the near-field (NF) samples, which, owing to the rail imperfections, result in not being acquired over the measurement cylinder surface. The latter exploits an iterative scheme to restore the samples at the sampling points required by the adopted NR representation along the scan helix from those obtained by applying the CW correction technique and impaired by 2D mispositioning errors. The so compensated NF samples are then effectively recovered via a 2D optimal sampling interpolation (OSI) scheme to accurately obtain the input data required to carry out the standard cylindrical NTFF transformation. The OSI representation is determined here by assuming a long antenna under test as enclosed in a prolate ellipsoid or cylinder ending into two hemispheres (cigar) in order to make, depending on the particular geometry of the considered antenna, the representation effectively non-redundant. The reported numerical simulation results show the capability of the proposed approach to compensate even severe 3D mispositioning errors, thus enabling its usage in a real measurement scenario.

Keywords: antenna measurements; near to far-field transformations; non-redundant sampling representation; helicoidal scanning; probe mispositioning errors compensation



Citation: D'Agostino, F.; Ferrara, F.; Gennarelli, C.; Guerriero, R.; Migliozi, M.; Pascarella, L.; Riccio, G. Three-Dimensional Probe Mispositioning Errors Compensation: A Feasibility Study in the Non-Redundant Helicoidal Near to Far-Field Transformation Case. *Electronics* **2024**, *13*, 3767. <https://doi.org/10.3390/electronics13183767>

Academic Editors: Felipe Jiménez, Francisco Falcone, Sotirios K. Goudos, Sandra Costanzo, Flavio Canavero and Niamat Hussain

Received: 22 July 2024

Revised: 28 August 2024

Accepted: 19 September 2024

Published: 22 September 2024



Copyright: © 2024 by the authors. Licensee MDPI, Basel, Switzerland. This article is an open access article distributed under the terms and conditions of the Creative Commons Attribution (CC BY) license (<https://creativecommons.org/licenses/by/4.0/>).

1. Introduction

Antennas are becoming more and more sophisticated to meet the needs of increasingly demanding technical applications. This leads to an increasing requirement for more advanced testing techniques in order to verify their performance. Several factors are involved in the choice between outdoor or indoor far-field (FF) and near-field (NF) setups and between different adopted scanning types: frequency, electrical size, application, measurement specifications, FF angular coverage, environmental and security requirements, and other factor (i.e., weight and physical dimension). Nowadays, NF antenna measurements are becoming more and more a fundamental tool, since they represent a valuable alternative to classical FF measurements, when weather and security do not permit the option of an outdoor FF range or the FF conditions cannot be satisfied in an indoor FF setup and when the complete pattern and polarization measurements are required [1–10].

In such a case, the antenna far-field is achieved by using near to FF (NTFF) transformation techniques, which particularize depending on the specific NF scanning facility adopted for the data collection, which, therefore, can be with planar, cylindrical, or spherical scan. Among these techniques, that using cylindrical scan [11–21] is particularly advisable when characterizing a low-directivity fan beam pattern antenna under test (AUT), as those used in the base stations of the modern mobile communication networks [22] or body-centric communication systems [23].

Over the years, researchers and technicians have spent many resources to meet the ever-growing demand of advanced antenna measurement techniques. A significant contribution to the reaching of this aim has been offered by the exploitation of the non-redundant (NR) sampling representations of the electromagnetic (EM) field [24]. As a matter of fact, by applying them to suitably represent the voltage detected at the scanning probe terminals, effective cylindrical NTFF transformations [15], requiring the collection of a drastically reduced amount of NF data with regard to those required by the classic cylindrical transformation [11–13], have been proposed. The NR sampling approach, unlike the classical one, is characterized by sampling rings, whose distances increase when going from the center of the measurement cylinder to its peripheral zones, whilst the number of samples on them decreases. Then, the classical NTFF transformation [11,13] is performed after recovering, from the acquired NR samples, the required equally spaced NF data by means of an optimal sampling interpolation (OSI) expansion of the central type.

Taking the hint of Yaccarino et al. [25], an additional reduction of measurement time has been obtained in [26,27] by contriving NR NTFF transformations with a helicoidal scan for long AUTs, wherein the NF data are acquired on-the-fly by synchronizing the continuous motions of the AUT and probe positioners. Such techniques, unlike that in [28], arise from the results on the unified theory of spiral scans for non-volumetric antennas [29] and adopt a prolate ellipsoid [26] or a cigar [27], i.e., a cylinder terminated by two hemispheres, to model the considered AUT and effectively devise the NR representation of the probe voltage along the scanning helix. Moreover, they adopt an ad-hoc 2D OSI formula to obtain the input NF data for the classical NTFF transformation [11,13].

Unfortunately, the measurements of the NF samples exactly at the locations determined by the utilized NR sampling representation can be impaired by the imprecise control of the AUT and probe positioners and/or by their low resolution as well as by the inaccurate synchronization of their continuous movements when drawing the scan helix. In addition, the rails that drive the linear movement of the probe may be impaired by the poor mechanical precisions, and this might make the radius at which any NF sample is actually acquired different from the nominal scanning cylinder one. The gathered NF samples are, therefore, corrupted by 3D positioning errors, whose amount could actually be detected using optical devices through interferometric methods. On the other hand, if the scan helix is drawn by an unmanned aerial vehicle [30,31] in an outdoor environment, the weather conditions and limited resolution of inertial navigation systems may prevent the preservation of the preset flight trajectory [32]. Nevertheless, GPS can provide the information on the actual sampling points, thus allowing one, as in the indoor case, the 3D mispositioning errors to be considered known. A matrix formulation-based approach has been proposed in [33–35] to correct such types of errors affecting the standard NTFF transformations using the plane-rectangular, cylindrical, and spherical scans. In any case, it cannot be conveniently applied in the case of the here-adopted NTFF transformation with the helicoidal scan.

Recently, these types of errors affecting the NR planar [36] and cylindrical [37] NTFF transformations have been properly compensated for by developing two-step procedures whose first step is similar to that proposed in [38].

This article aims to carry out a feasibility study on the compensation of 3D mispositioning errors affecting the helicoidal NTFF transformations [26,27]. To this end, the use of the two-step technique in [37] is suitably extended to correct such types of errors affecting the collection of the NR helicoidal samples. Accordingly, in the former step, a

proper phase correction, the cylindrical wave (CW) correction [37], is applied to correct the phase errors owing to the acquisition of the helicoidal NF samples at radii different from that of the nominal scan cylinder. The so restored NF samples, which now lie on the correct measurement surface, are corrupted by 2D mispositioning errors only. These 2D errors are supposed to be such that it is always possible to associate each NF sample at the correct sampling point to that at the nearest mispositioned point. Such an assumption is certainly fulfilled if the mispositioning error sources are those realistically considered here. Therefore, in the latter step, the iterative scheme, developed and experimentally validated in [39,40], is applied to restore the correctly positioned helicoidal NF samples from the 2D mispositioned ones.

This article is structured as follows. First, the key results, to obtain an efficient sampling representation of the voltage gathered by a non-directive probe on the scanning helix, and the 2D OSI formula, allowing the recovery of the voltage at any point on the measurement cylinder from a NR amount of its helicoidal samples, are summarized in Section 2. The two-step method able to compensate for the 3D probe positioning errors, preventing the acquisition of the helicoidal NF samples at the points dictated by the prolate ellipsoid or cigar-based NR representation, is devised in Section 3. Numerical results are shown in Section 4 to appraise the efficacy of the proposed correction procedure. Finally, conclusions are collected in Section 5.

2. OSI Representation over a Helix

As shown in Figure 1, depicting the geometry of the problem in a 0xyz reference system, a long AUT is characterized in a cylindrical NF setup through a helicoidal scanning, to make the NF measurement speedier. The NR representation of the voltage gathered by the chosen non-directive probe is developed according to the results in [26,27], properly exploiting the theoretical background on the unified theory of NR spiral scans for non-volumetric AUTs [29]. Accordingly, a long AUT is considered as surrounded in a convex domain limited by a rotational surface Σ that, depending on its geometry, can be a prolate ellipsoid of minor and major semi-axes equal to b' and a' or a so-called cigar, as it is obtained by a cylinder of radius a_c and height h_c , ending into two hemispheres (see Figure 2). From the volumetric redundancy reduction standpoint, the prolate ellipsoid is suitably chosen if the given AUT does not have a regular shape but shows a maximum in the central region of its transverse section; otherwise, the cigar represents the best choice [26,27].

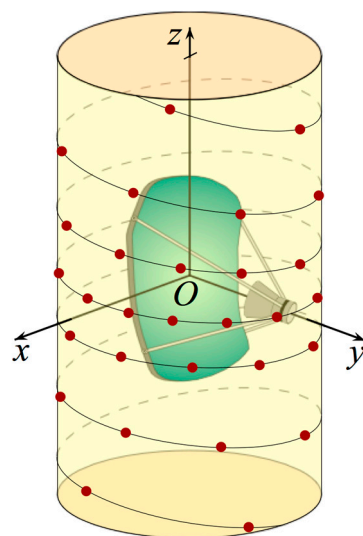


Figure 1. Characterization of a long AUT through a helicoidal NF setup.

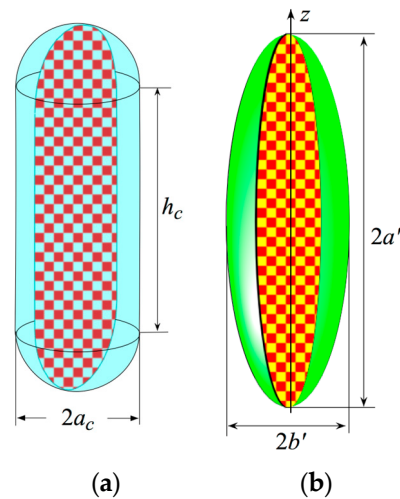


Figure 2. (a) Cigar. (b) Prolate ellipsoid.

It has been demonstrated in [41] that the effective spatial bandwidths of the voltage V revealed by the scan probe and the field radiated by the AUT coincide. This result enables the application of the NR sampling representations of the EM field [24], according to which V can be suitably represented by the “reduced voltage” \tilde{V} . This last is obtained by describing any curve on the scan cylinder via an optimal parameter, say μ , and by extracting from the expression of the voltage $V(\mu)$ a phase factor $e^{-j\psi(\mu)}$, with $\psi(\mu)$ being a suitably determined phase function. Thus, \tilde{V} , referring to the voltage detected either by probe (V_1) or by the rotated probe (V_2), is defined as

$$\tilde{V}(\mu) = \tilde{V}_{1,2}(\mu) = V_{1,2}(\mu)e^{j\psi(\mu)}. \tag{1}$$

$\tilde{V}(\mu)$ is a spatially quasi-bandlimited function but can approach a strictly spatially bandlimited function by enlarging its bandwidth W_μ by an excess factor χ' [24], determined such that the related band limitation error results negligible. Usually, excess factors slightly greater than the unity are utilized in the case of AUTs, which are large in term of the wavelength λ [24].

Let us turn now to the determination of the scan helix and to the development of the NR representation over it, which allows the recovery of the voltage value at any point on the measurement cylinder through an effective 2D OSI algorithm. The helicoidal trajectory is suitably determined by projecting onto the scan cylinder of radius d the spiral which enfolds the surface Σ with a pitch equal to the sample spacing necessary for interpolating on the cylinder generatrices. The NR representation over this helix is then devised according to a heurist reasoning which parallelizes the exact one obtained when adopting a spherical modeling of the AUT [29].

By choosing the following as the spatial bandwidth,

$$W_\mu = \frac{\uparrow(C')}{\lambda}, \tag{2}$$

with C' being the curve obtained by intersecting Σ with the meridian plane that passes across the observation point P and its length $\uparrow(C')$, the phase function and the optimal parameter representing a cylinder generatrix can be expressed as

$$\mu = (\pi/\uparrow(C')) [D_{PP_1} + s'(P_1) - D_{PP_2} + s'(P_2)] \tag{3}$$

$$\psi = (\pi/\lambda) [D_{PP_1} + s'(P_1) + D_{PP_2} - s'(P_2)] \tag{4}$$

where D_{PP_1} and D_{PP_2} are the distances between P and the tangency points P_1 and P_2 on C' , respectively, and $s'(P_1)$ and $s'(P_2)$ are their arc length abscissas.

Relations (2), (3), and (4) particularize depending on whether the cigar or the prolate ellipsoid is chosen as the AUT modeling.

When adopting the cigar, $\uparrow(C') = 2(h_c + \pi a_c)$ and the parameters involved in (3) and (4) can be determined (see Figure 3) via the following [27]:

$$D_{PP_{1,2}} = \sqrt{(z h_c/2)^2 + d^2 - a_c^2}; s'(P_1) = a_c \sin^{-1} \left(\frac{a_c d + D_{PP_1}((h_c/2) - z)}{D_{PP_1}^2 + a_c^2} \right) \quad (5)$$

$$s'(P_2) = h_c + a_c \left[\pi - \sin^{-1} \left(\frac{a_c d + D_{PP_2}((h_c/2) + z)}{D_{PP_2}^2 + a_c^2} \right) \right] \quad (6)$$

When adopting the prolate ellipsoid, $\uparrow(C') = 4a'E(\pi/2|\kappa^2)$ and relations (3) and (4) can be rewritten as [26]

$$\mu = \frac{\pi}{2} \left[1 + \frac{E(\sin^{-1} v'|\kappa^2)}{E(\pi/2|\kappa^2)} \right]; \psi = \frac{2\pi a'}{\lambda} \left[v \sqrt{\frac{u'^2 - 1}{u'^2 - \kappa^2}} - E \left(\cos^{-1} \sqrt{\frac{1 - \kappa^2}{u'^2 - \kappa^2}}|\kappa^2 \right) \right] \quad (7)$$

where $E(\bullet|\bullet)$ denotes the elliptic integral of the second kind, $\kappa = f/a'$ is the eccentricity of the ellipse obtained as the intersection of a meridian plane with the ellipsoidal modeling surface Σ , $2f$ is its focal distance, $u' = (d_1 + d_2)/2a'$, $v' = (d_1 - d_2)/2f$ are the related elliptic coordinates, with $d_{1,2}$ being the distances from P to the foci of the ellipse.

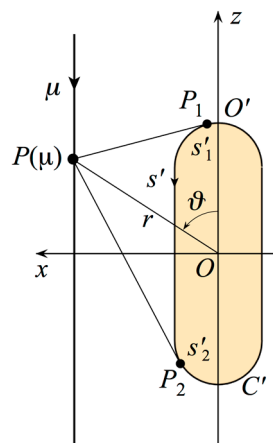


Figure 3. Relevant to the determination of μ and ψ in the case of the cigar modeling.

The equations of the scan helix, by forcing its passage through a point P_0 of the cylinder generatrix at $\phi = 0$, are [26,27]

$$\begin{cases} x = d \cos(\phi - \phi_s) \\ y = d \sin(\phi - \phi_s) \\ z = d \cot[\vartheta(\mu)] \end{cases} \quad (8)$$

where ϕ is the angular parameter describing the helix, ϕ_s is its value at P_0 , and $\mu = k\phi$, with k fixing the helix step. This last is determined such that it is equal to the sample spacing $\Delta\mu = 2\pi/(2M'' + 1)$ on a generatrix, where $M'' = \lfloor \chi M' \rfloor + 1$ and $M' = \lfloor \chi' W_\mu \rfloor + 1$, $\lfloor \cdot \rfloor$ symbolizes the floor function, and χ is an oversampling factor [24]. Therefore, $k = 1/(2M'' + 1)$.

As regards the determination of the NR representation along the scan helix, the parameter σ describing it and the related phase function γ , as well as bandwidth W_σ , can be attained as shown in [26,27,29]. In particular, since the helix is achieved as a projection of the spiral enfolding Σ via the curves at $\mu = \text{const}$, σ has to be related to the curvilinear abscissa s of the corresponding point on the projecting spiral according to the constant

$2\pi/(\lambda W_\sigma)$. The related phase function γ is obtained by assuming any helicoidal sampling point as belonging to the generatrix passing through it; thus, γ equals ψ . The bandwidth W_σ is instead related to the arclength of the spiral enfolding Σ from pole to pole by the constant $2/\lambda$.

The voltage value can then be recovered, from a NR number of samples gathered along the helix, at any point, P , on the scan cylinder surface, by using the following 2D OSI formula:

$$V(\mu(\vartheta), \varphi) = e^{-j\psi(\mu)} \sum_{m=m_0-p+1}^{m_0+p} \{OSF(\mu, \mu_m, \bar{\mu}, M, M'') \sum_{n=n_0-q+1}^{n_0+q} \tilde{V}(\sigma_n) OSF(\sigma(\mu_m), \sigma_n, \bar{\sigma}, N, N'')\} \quad (9)$$

where $2p \times 2q$ is the number of the nearest samples retained in the interpolation, and

$$\mu_m = \mu_m(\varphi) = \mu(\phi_s) + k\varphi + m\Delta\mu = \mu_0 + m\Delta\mu; \sigma_n = \sigma(\phi_s) + n\Delta\sigma = \sigma_s + 2\pi n/(2N'' + 1) \quad (10)$$

$$N'' = \lfloor \chi N' \rfloor + 1; N' = \lfloor \chi' W_\sigma \rfloor + 1; N = N'' - N'; M = M'' - M' \quad (11)$$

$$m_0 = \lfloor (\mu - \mu_0)/\Delta\mu \rfloor; n_0 = \lfloor (\sigma - \sigma_s)/\Delta\sigma \rfloor. \quad (12)$$

Moreover,

$$OSF(\alpha, \alpha_\dagger, \bar{\alpha}, K, K'') = D_{K''}(\alpha - \alpha_\dagger) \Omega_K[(\alpha - \alpha_\dagger), \bar{\alpha}] \quad (13)$$

is the OSI function, wherein

$$\Omega_K(\alpha, \bar{\alpha}) = \frac{T_K[2 \cos^2(\alpha/2)/\cos^2(\bar{\alpha}/2) - 1]}{T_K[2/\cos^2(\bar{\alpha}/2) - 1]}; D_{K''}(\alpha) = \frac{\sin[(2K'' + 1)\alpha/2]}{(2K'' + 1) \sin(\alpha/2)} \quad (14)$$

are the Tschebyscheff sampling and Dirichlet functions [24,26,27,29], respectively, $T_K(\cdot)$ being the K th-degree Tschebyscheff polynomial.

3. From 3D Probe Positioning Errors Affected Data to NR Helicoidal Samples

Regardless of the modeling used to develop the NR OSI representation, the positions of the collected helicoidal NF samples are supposed to be impaired by 3D probe mispositioning errors as a result of the imperfections in the rail driving the linear movement of the probe and inaccurate synchronization of the probe motion with that of the AUT when drawing the scan helix. Moreover, the actual position is assumed to be known, since it can be detected by optical devices. Under these hypotheses, the mispositioning 3D errors can be successfully compensated for by adopting the following two-step approach (see Figure 4).

In the former step, the CW phase correction [37] is exploited to correct the radial deviations of the collected samples with respect to the radius of the nominal scan cylinder. Accordingly, by denoting the shifts of the collected voltage samples from the scan cylinder by $\delta\rho_v, v = 1, \dots, N_{HS}$, with N_{HS} being the number of the collected NR helicoidal samples, the samples at the exact radial coordinate d can be restored via

$$V(d, \varphi, z) = V(d + \delta\rho_v, \varphi, z) e^{j2\pi\delta\rho_v/\lambda} \quad (15)$$

where $V(d + \delta\rho_v, \varphi, z)$ are the samples impaired by 3D position errors.

The so retrieved samples now belong to the nominal scan cylinder, but they still remain to be affected by 2D mispositioning errors. To compensate for these errors, an iterative algorithm [39,40] is applied in the latter step, as long as a biunique relationship, allowing one to associate at each uniform sampling point σ_i the “closest” non-uniform one (ζ_i, ε_i) , can be reliably built. Taking into account the sources of the probe mispositioning errors, this hypothesis is surely verified. The OSI expansion (9) can be applied to relate the value of each of the voltage samples erroneously collected at each (ζ_i, ε_i) to those of the unknown samples at the nearest uniform sampling points, thus obtaining a linear system:

$$\tilde{V}(\zeta_i, \varepsilon_i) = \sum_{m=m_0-p+1}^{m_0+p} \left\{ OSF(\zeta_i, \mu_m, \bar{\mu}, M, M'') \sum_{n=n_0-q+1}^{n_0+q} \tilde{V}(\sigma_n) OSF(\sigma(\mu_m), \sigma_n, \bar{\sigma}, N, N'') \right\}. \quad (16)$$

In order to adopt an iterative scheme to solve the linear system (16) in the unknown $\tilde{V}(\sigma_i)$, it is convenient to rearrange it in the following matrix form:

$$\underline{W}\underline{U} = \underline{C}, \quad (17)$$

with \underline{U} being the column vector of the unknown NF helicoidal samples, \underline{C} the column vector of the NF samples obtained at the first step by applying the CW phase correction, and \underline{W} a $N_{HS} \times N_{HS}$ -sized matrix, having the OSI formula weight function as its elements and to split the matrix \underline{W} in terms of its diagonal \underline{W}_D and not diagonal $\underline{\Delta}$ parts. The iterative scheme is then obtained by rearranging the terms of the resulting matrix equation, multiplied on both sides by \underline{W}^{-1} , as

$$\underline{U}^{(j)} = \underline{W}_D^{-1}\underline{C} - \underline{W}_D^{-1}\underline{\Delta}\underline{U}^{(j-1)} = \underline{U}^{(0)} - \underline{W}_D^{-1}\underline{\Delta}\underline{U}^{(j-1)} \quad (18)$$

with $\underline{U}^{(j)}$ being the vector of the restored samples at the j th iteration.

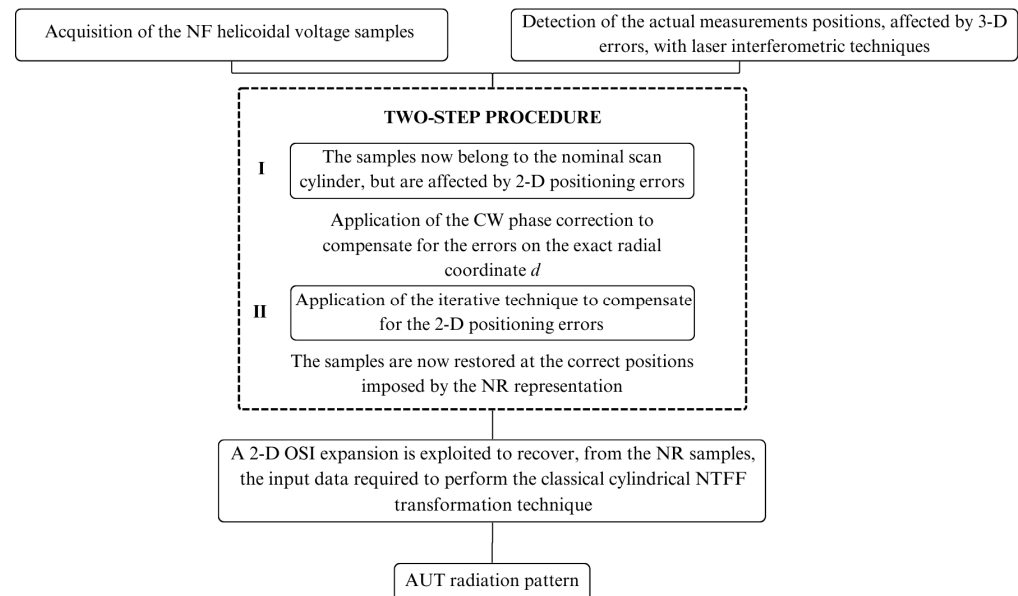


Figure 4. Representative flowchart of the two-step technique.

Taking into account the hypothesis relevant to the non-uniform samples distribution, the necessary conditions for the convergence of the iterative relation, requiring that the magnitude of each element on the main diagonal of \underline{W} be different from zero and greater than the magnitudes of the other elements on the same row or column [39,40], are surely fulfilled. Furthermore, (18) can be explicitly expressed as

$$\tilde{V}^{(j)}(\sigma_i) = \frac{1}{DEN} \left\{ \tilde{V}(\zeta_i, \varepsilon_i) - \sum_{m=m_0-p+1}^{m_0+p} OSF(\zeta_i, \mu_m, \bar{\mu}, M, M'') \times \sum_{\substack{n=n_0-q+1 \\ n \neq i}}^{n_0+q} \tilde{V}^{(j-1)}(\sigma_n) OSF(\sigma(\mu_m), \sigma_n, \bar{\sigma}, N, N'') \right\} \quad (19)$$

where

$$DEN = OSF(\zeta_i, \mu_{m_i}, \bar{\mu}, M, M'') OSF(\sigma(\mu_{m_i}), \sigma_i, \bar{\sigma}, N, N'') \quad (20)$$

with $m_i = \lfloor (\zeta_i - \mu_0) / \Delta\mu \rfloor$.

Once the NF samples have been restored at the points imposed by the NR representation along the helix based on the use of either the prolate ellipsoid or the cigar, they can be interpolated via relation (9) to determine the NF data at the points of the cylindrical equispaced lattice, whose knowledge allows performing the standard NTFF transformation [11,13] with compensation of the probe effects.

4. Numerical Assessment

A lot of numerical simulations have been performed in order to verify the capability of the proposed approach to compensate for 3D mispositioning errors, which impair the antenna characterization of a long antenna in an anechoic chamber provided with a helicoidal scan system. The results, reported in the following section, refer to two distinct simulated AUTs, which, due to their geometric features, are modeled using a prolate ellipsoid or a cigar. Note that these results are independent of the kind of the considered AUT, since the approach requires, as a priori information, only the knowledge of its geometry.

The former example (CASE 1) is relevant to an ideal long antenna with a non-regular shape. To this end, a uniform planar array, lying in the xz -plane and covering an ellipse shape, with minor and major semi-axes equal to equal to 6λ and 20λ , has been considered. Its elements are z -polarized Huygens sources, spaced by 0.7λ along x and 0.8λ along z . As such an array shows a maximum in the central region of its transverse section, a prolate ellipsoid with $b' = 6\lambda$ and $a' = 20\lambda$ has been utilized to effectively model it.

The latter example (CASE 2) refers to an ideal long AUT now having a regular shape. In such a case, a uniform planar array of elementary Huygens sources, lying in the xz -plane and covering a surface made by a $14\lambda \times 28\lambda$ rectangle ending into two hemicircles with a radius of 7λ , has been simulated. The array elements are, again, polarized along the z -axis but are now 0.7λ and 0.8λ spaced along z and x , respectively. A cigar, having $a_c = 7\lambda$ and $h_c = 28\lambda$, has been employed to obtain an effective NR representation over the scan helix.

In both cases, the NF measurements have been simulated as gathered by an open-ended rectangular waveguide operating the X-band center frequency [42] along a proper helix enfolding a cylinder with the following dimensions: $d = 12\lambda$ and $h = 120\lambda$. Moreover, the sampling points have been considered as impaired by known 3D position errors, as it occurs in real measurements. In particular, the radial coordinate of each of the σ_n helicoidal sampling points has been modeled as a random variable uniformly distributed in the range $[d - 0.07\lambda, d + 0.07\lambda]$. Also, the position $(\sigma, \mu(\sigma))$ of each of them deviates from the exact one, and the shift has been modeled as a random variable uniformly distributed in $[-0.3\Delta\sigma, 0.3\Delta\sigma]$ and $[-0.3\Delta\mu, 0.3\Delta\mu]$.

The efficacy of the devised compensation procedure has been verified by comparing the exact NF patterns with those reconstructed from the helicoidal NF samples impaired by 3D mispositioning errors. Representative examples relevant to reconstructions of amplitudes and phases of the voltages along the generatrix at $\varphi = 90^\circ$ are shown in Figure 5 for the AUT considered in the CASE1 and in Figure 6 for that of the CASE2. For the sake of completeness, the comparisons relevant to the generatrix at $\varphi = 60^\circ$ are shown in the Figure 7 for the AUT of the CASE1 and Figure 8 for that of CASE2. As can be seen, the error compensation obtained by using the CW correction in (15) followed by the iterative technique works well, and, although the considered mispositioning errors are large, it allows for quite accurate NF recoveries, as compared to those achieved by the direct interpolation of the mispositioned NF samples, which, on the contrary, result in being significantly deteriorated. Note that 10 iterations have been found sufficient [39,40] for the iterative scheme (18) to converge. It must be stressed that the application of the first step, namely, the CW phase correction, is straightforward and not time-consuming. Also, the application of the iterative technique requires very short times. For instance, the 10 iterations required for the convergence of the iterative algorithm have taken 14.5 and

8.5 s in the CASE 1 and CASE 2, respectively, on an old Apple MacBook provided with an Intel Core I7 processor @1.7 GHz.

To underline the need to adopt both the steps of the developed procedure, Figure 9 shows, in both cases, a representative recovery of the voltage amplitudes on the generatrix at $\varphi = 90^\circ$, attained by applying only the CW phase correction, whilst Figure 10 refers to the reconstructions of their phases obtained by using only the iterative technique. According to the shown results, it should be evident that the CW correction has to be necessarily combined with the iterative technique to attain an accurate 3D mispositioning errors compensation. To stress the robustness of the two-step procedure, the amplitudes and phases of the voltage samples, already impaired by 3D positioning errors, have been altered also by a background noise with arbitrary phase and amplitude limited to $\Delta\alpha$ and an uncertainty of $\pm\Delta A_r$ in amplitude and $\pm\Delta\eta_r$ in phase to simulate an actual measurement performed in an anechoic chamber.

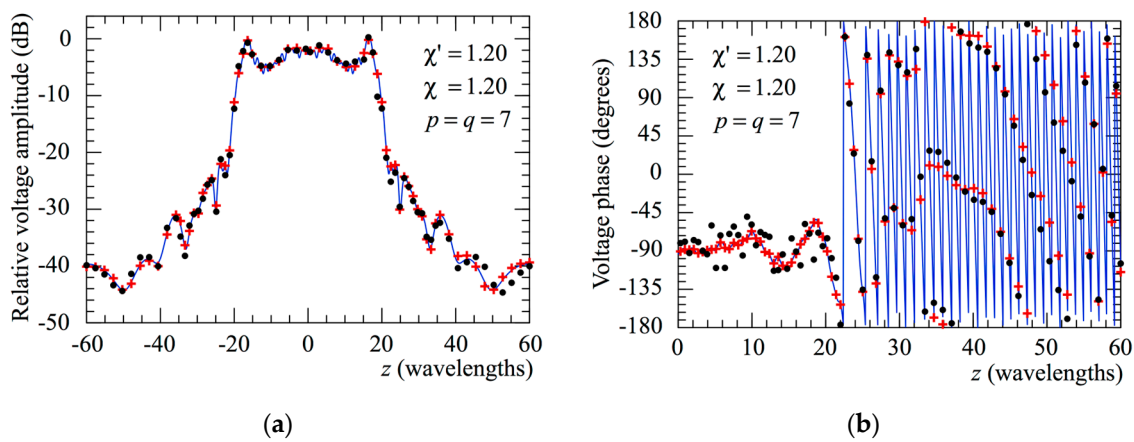


Figure 5. CASE 1. Voltage on the generatrix at $\varphi = 90^\circ$. — exact. + + + + obtained from the mispositioning errors impaired NF samples by using the two-step procedure. • • • • achieved from the positioning errors corrupted NF samples without performing the two-step procedure: (a) Amplitude; (b) Phase.

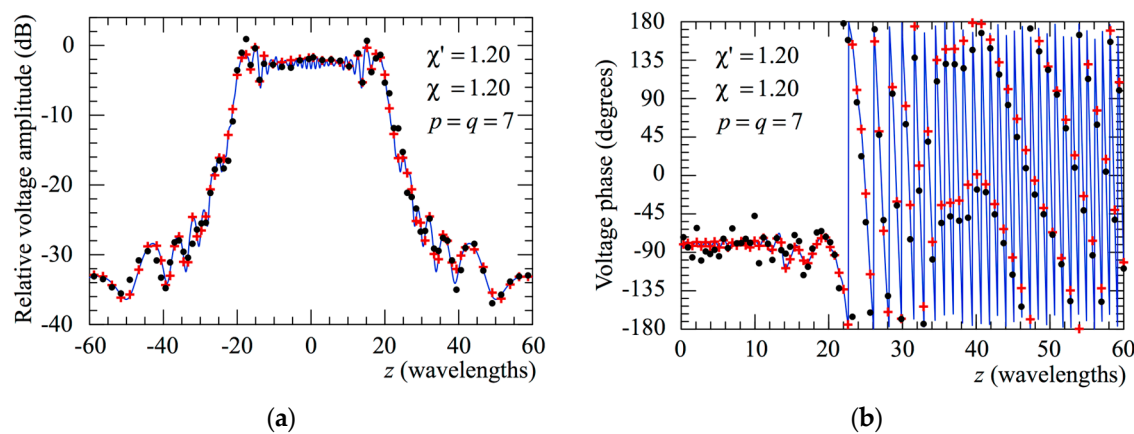


Figure 6. CASE 2. Voltage on the generatrix at $\varphi = 90^\circ$. — exact. + + + + obtained from the mispositioning errors impaired NF samples by using the two-step procedure. • • • • achieved from the positioning errors corrupted NF samples without performing the two-step procedure: (a) Amplitude; (b) Phase.

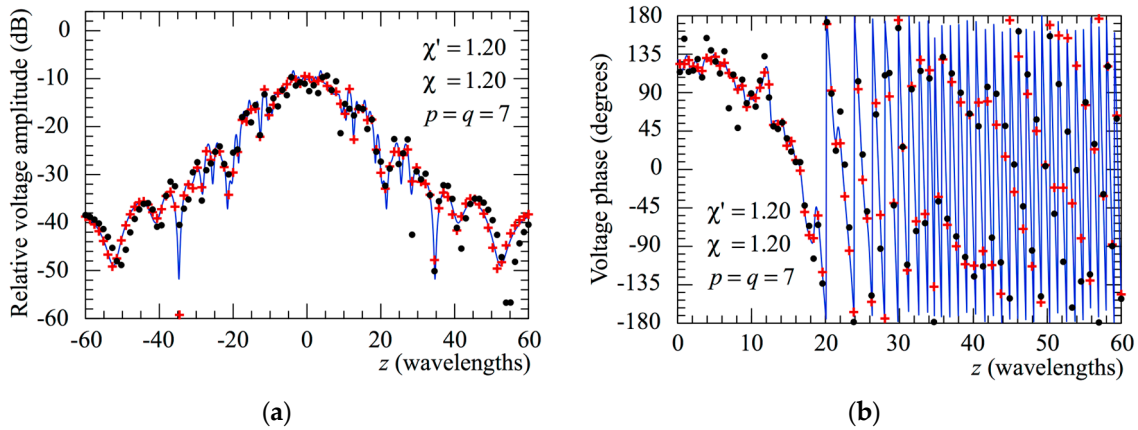


Figure 7. CASE 1. Voltage on the generatrix at $\varphi = 60^\circ$. — exact. + + + + obtained from the mispositioning errors impaired NF samples by using the two-step procedure. • • • • achieved from the positioning errors corrupted NF samples without performing the two-step procedure: (a) Amplitude; (b) Phase.

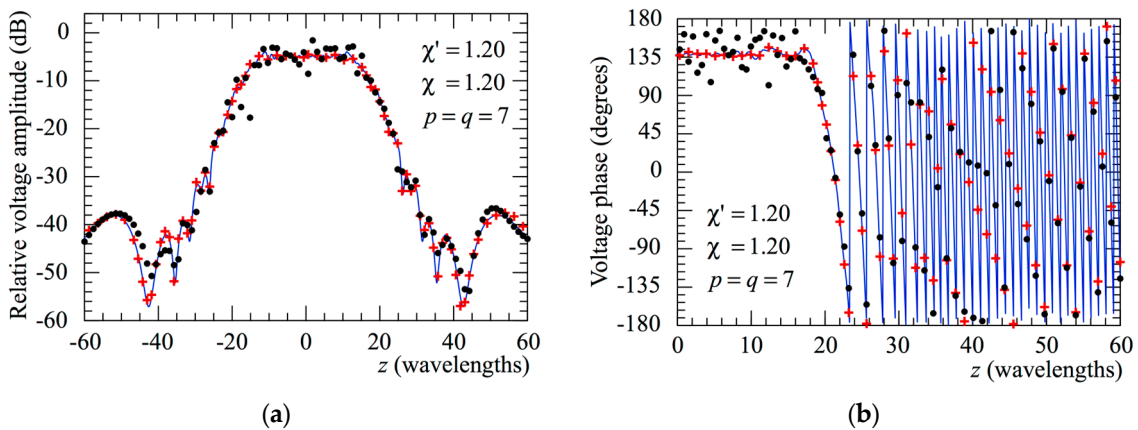


Figure 8. CASE 2. Voltage on the generatrix at $\varphi = 60^\circ$. — exact. + + + + obtained from the mispositioning errors impaired NF samples by using the two-step procedure. • • • • achieved from the positioning errors corrupted NF samples without performing the two-step procedure: (a) Amplitude; (b) Phase.

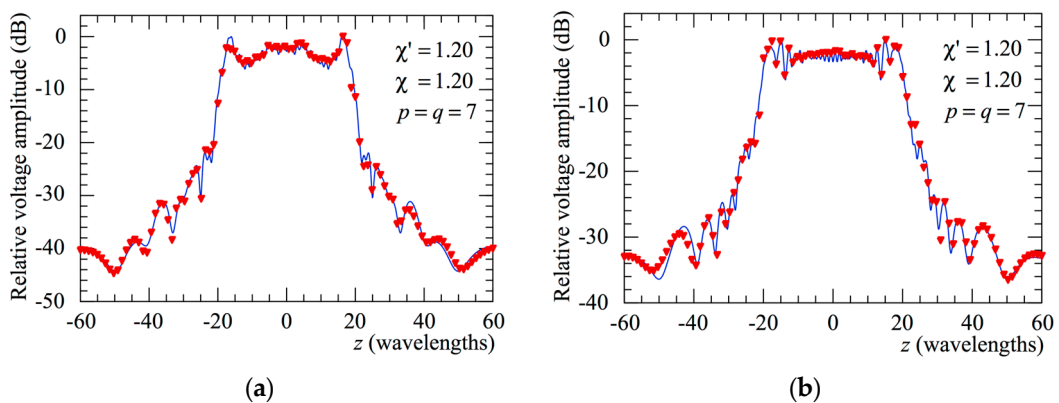


Figure 9. Voltage amplitude on the generatrix at $\varphi = 90^\circ$. — exact. ▼▼▼▼ obtained from the positioning errors corrupted NF samples by performing only the CW phase correction: (a) CASE 1; (b) CASE 2.

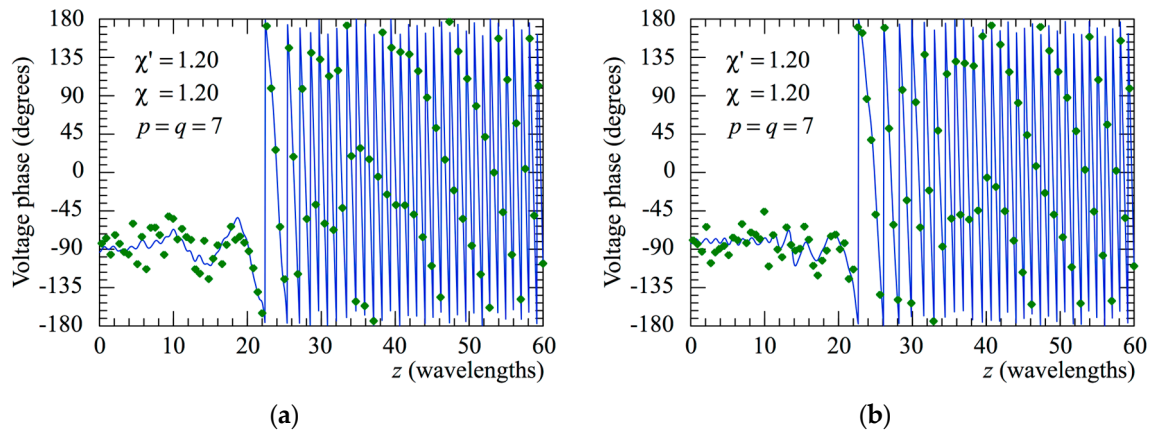


Figure 10. Voltage phase on the generatrix at $\varphi = 90^\circ$. — exact. ◆◆◆◆ obtained from the positioning errors NF samples by performing only the iterative procedure: (a) CASE 1; (b) CASE 2.

Figure 11a (CASE1) and Figure 11b (CASE2) show the reconstructions of voltage amplitude at $\varphi = 90^\circ$ obtained from these samples affected by both the error sources. As can be seen, the procedure results are stable even in a real measurement environment.

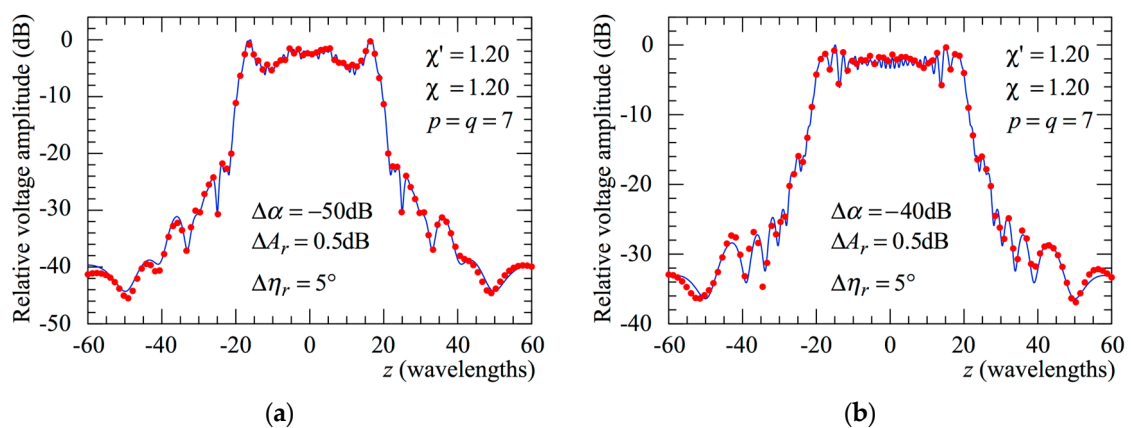


Figure 11. Voltage amplitude on the generatrix at $\varphi = 90^\circ$. — exact. ●●●● obtained from the positioning and measurement errors altered NF samples by using the two-step procedure. (a) CASE 1; (b) CASE 2.

At last, the E- and H- plane FF patterns reconstructed from the errors corrupted samples by using the described procedure are compared in Figure 12 (CASE1) and in Figure 13 (CASE2) with the exact ones and with those obtained without applying it. As can be seen, very satisfying recoveries result when applying the two-step procedure, whilst those obtained, wherein it is not applied, appear severely deteriorated. The necessity to employ the iterative technique after the CW phase correction to effectively compensate for the 3D position errors is demonstrated in Figures 14 and 15 for CASE1 and CASE2, respectively, where it is shown the FF reconstruction in the E- and H- plane obtained by applying only the CW phase correction (see red triangles). On the other hand, the application of the iterative technique is not sufficient to obtain accurate reconstructions (see green rhombi), thus justifying the need to perform both steps.

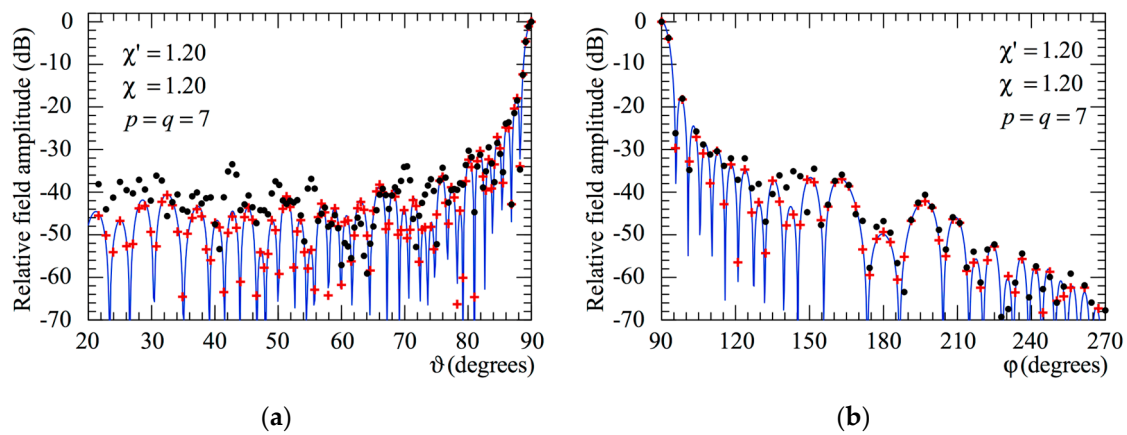


Figure 12. CASE 1. FF patterns in the principal planes. — exact. + + + + obtained from the positioning errors corrupted NF samples by using the two-step procedure. ● ● ● ● attained from the positioning errors altered NF samples without the two-step procedure: (a) E-Plane; (b) H-plane.

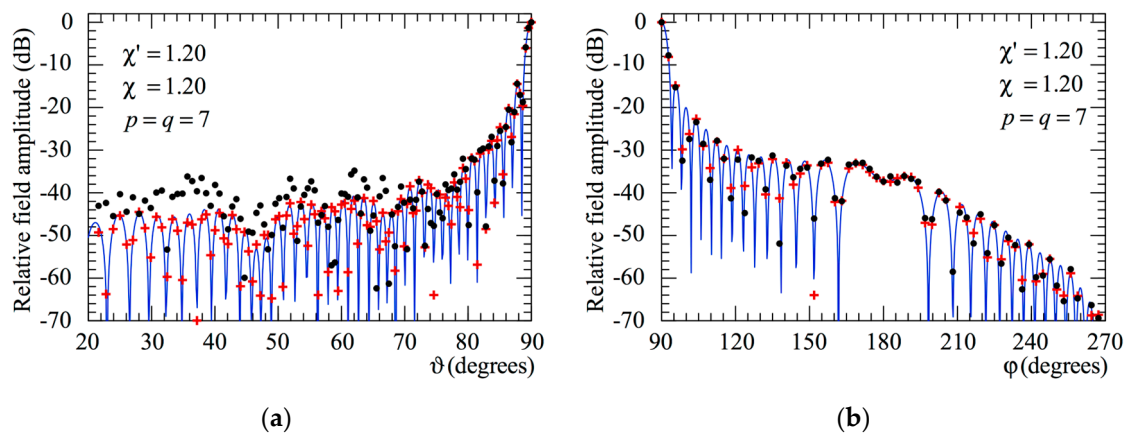


Figure 13. CASE 2. FF patterns in the principal planes. — exact. + + + + obtained from the positioning errors corrupted NF samples by using the two-step procedure. ● ● ● ● attained from the positioning errors altered NF samples without the two-step procedure: (a) E-Plane; (b) H-plane.

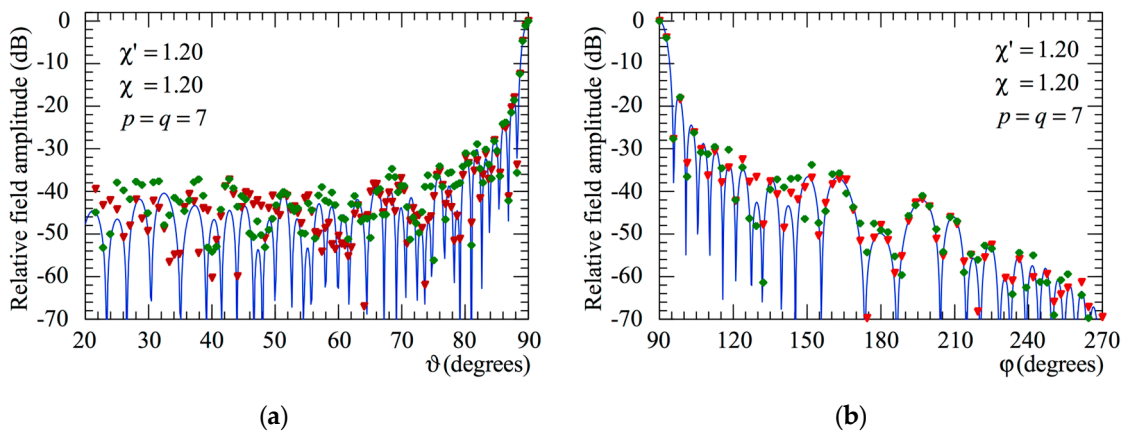


Figure 14. CASE 1. FF patterns in the principal planes. — exact. ▼ ▼ ▼ ▼ obtained from the position errors corrupted NF samples using only the CW correction. ◆ ◆ ◆ ◆ obtained from the position errors corrupted NF samples using only the iterative technique. (a) E-Plane; (b) H-plane.

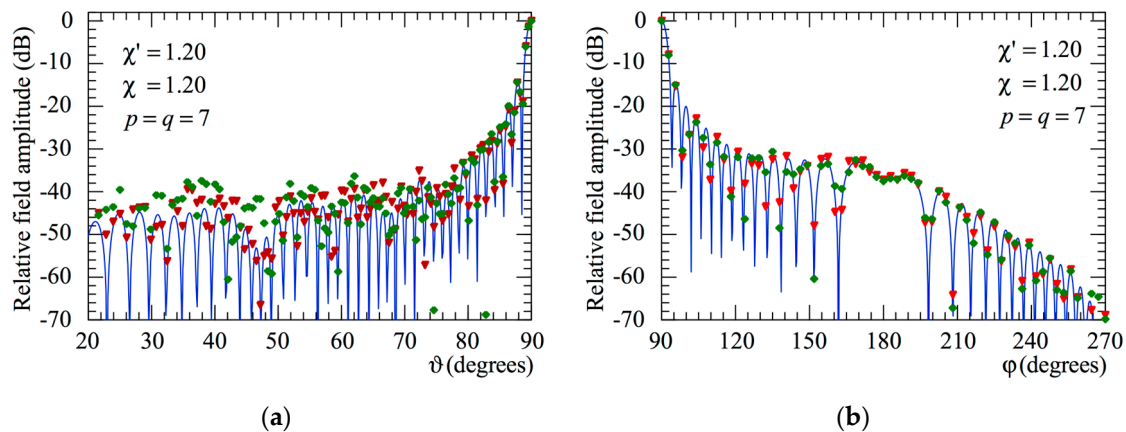


Figure 15. CASE 2. FF patterns in the principal planes. — exact. ▼▼▼▼ obtained from the position errors corrupted NF samples using only the CW correction. ◆◆◆◆ obtained from the position errors corrupted NF samples using only the iterative technique. (a) E-Plane; (b) H-plane.

Finally, it is noteworthy that the number of employed helicoidal NF samples is 13,162 for CASE1 and 15,312 for CASE2, hence, much smaller than that (30,720) needed by the classical Leach and Paris's NTF transformation [11,13].

5. Concluding Remarks

In this paper, a feasibility study on possibility to compensate for 3D probe mispositioning errors in a NR helicoidal NTF transformation for long AUTs, using either a prolate ellipsoid or a cigar to model them, has been carried out. To this end, an effective approach has been proposed. It requires two steps: the CW phase correction to correct the errors caused by the deviations of the NF samples from the nominal scan cylinder and the iterative technique to restore the correctly positioned samples from those obtained after the CW phase correction, which result in being affected by 2D mispositioning errors. The reported numerical results, relevant to the characterization of two distinct simulated AUTs from 3D probe mispositioning errors affected NF data, have thoroughly assessed the effectiveness of the developed procedure and the need to adopt both the CW correction and the iterative technique to achieve accurate NF and FF reconstructions. It must be stressed that the application of the two-step procedure takes a very short time, since the first step, namely, the CW phase correction, is straightforward and not time-consuming, whilst the iterations required for the convergence of the iterative technique take very few seconds, even on an old computer. A measurement campaign aiming to verify the feasibility of the approach also from the practical standpoint will start when the upgrade of the NF facility at the University of Salerno, required to make it possible, will be realized.

Author Contributions: Methodology, C.G. and R.G.; Software, C.G. and L.P.; Validation, F.D., F.F. and L.P.; Investigation, M.M.; Data curation, F.F.; Writing—original draft, R.G.; Writing—review & editing, F.F., C.G., R.G. and G.R.; Supervision, C.G. All authors have read and agreed to the published version of the manuscript.

Funding: This work was supported by the European Union under the Italian National Recovery and Resilience Plan (NRRP) of NextGenerationEU, partnership on “Telecommunications of the Future” (PE00000001—program “RESTART”, Structural Project MINDS DREAM).

Data Availability Statement: Data are contained within the article.

Conflicts of Interest: No conflict of interest is declared by the authors.

References

1. Yaghjian, A.D. An overview of near-field antenna measurements. *IEEE Trans. Antennas Propag.* **1986**, *34*, 30–45.
2. Appel-Hansen, J.; Dyson, J.D.; Gillespie, E.S.; Hickman, T.G. Antenna measurements. In *The Handbook of Antenna Design*; Rudge, A.W., Milne, K., Olver, A.D., Knight, P., Eds.; Peter Peregrinus: London, UK, 1986; pp. 584–694.

3. Gillespie, E.S. (Ed.) Special Issue on near-field scanning techniques. *IEEE Trans. Antennas Propag.* **1988**, *36*, 727–901.
4. Slater, D. *Near-Field Antenna Measurements*; Artech House: Boston, MA, USA, 1991.
5. Gregson, S.F.; McCormick, J.; Parini, C.G. *Principles of Planar Near-Field Antenna Measurements*; IET: London, UK, 2007.
6. Francis, M.H.; Wittmann, R.C. Near-field scanning measurements: Theory and practice. In *Modern Antenna Handbook*; Balanis, C.A., Ed.; John Wiley & Sons Inc.: Hoboken, NJ, USA, 2008; pp. 929–976.
7. *IEEE Standard 1720-2012*; IEEE Recommended Practice for Near-Field Antenna Measurements. Francis, M.H. (Ed.) IEEE: New York, NY, USA, 2012.
8. Sierra Castañer, M.; Foged, L.J. *Post-Processing Techniques in Antenna Measurement*; SciTech Publishing IET: London, UK, 2019.
9. Parini, C.; Gregson, S.; McCormick, J.; Van Resburg, D.J.; Eibert, T. *Theory and Practice of Modern Antenna Range Measurements*; SciTech Publishing IET: London, UK, 2020.
10. Ferrara, F.; Gennarelli, C.; Guerriero, R.; D'Agostino, F. *Non-Redundant Near-Field to Far-Field Transformation Techniques*; SciTech Publishing IET: London, UK, 2022.
11. Leach, W.M., Jr.; Paris, D.T. Probe compensated near-field on a cylinder. *IEEE Trans. Antennas Propag.* **1973**, *21*, 435–445.
12. Yaghjian, A.D. *Near-Field Antenna Measurement on a Cylindrical Surface: A Source Scattering Matrix Formulation*; NBS Tech. Note 696; U.S. Government Printing Office: Washington, DC, USA, 1977.
13. Joy, E.B.; Leach, W.M., Jr.; Rodrigue, G.P.; Paris, D.T. Applications of probe-compensated near-field measurements. *IEEE Trans. Antennas Propag.* **1978**, *26*, 379–389.
14. Appel-Hansen, J. On cylindrical near-field scanning techniques. *IEEE Trans. Antennas Propag.* **1980**, *28*, 231–234.
15. D'Agostino, F.; Ferrara, F.; Gennarelli, C.; Riccio, G.; Savarese, C. NF–FF transformation with cylindrical scanning from a minimum number of data. *Microw. Opt. Technol. Lett.* **2002**, *35*, 264–270. [[CrossRef](#)]
16. Hansen, T.B. Complex point sources in probe-corrected cylindrical near-field scanning. *Wave Motion* **2006**, *43*, 700–712. [[CrossRef](#)]
17. Hansen, T.B. Probe-corrected near-field measurements on a truncated cylinder. *J. Acoust. Soc. Am.* **2006**, *119*, 792–807. [[CrossRef](#)]
18. Hansen, T.B. Complex-point dipole formulation of probe-corrected cylindrical and spherical near-field scanning of electromagnetic fields. *IEEE Trans. Antennas Propag.* **2009**, *57*, 728–741. [[CrossRef](#)]
19. Qureshi, M.A.; Schmidt, C.H.; Eibert, T.F. Adaptive sampling in spherical and cylindrical near-field antenna measurements. *IEEE Antennas Propag. Magaz.* **2013**, *55*, 243–249. [[CrossRef](#)]
20. Sallucci, M.; Migliore, M.D.; Rocca, P.; Polo, A.; Massa, A. Reliable antenna measurements in a near-field cylindrical setup with a sparsity promoting approach. *IEEE Trans. Antennas Propag.* **2020**, *68*, 4143–4148. [[CrossRef](#)]
21. Kang, N.-W.; Lee, D.-J.; Kang, J.-S.; Kim, J.-H. Base-station antenna characterization by using cylindrical near-field scanning. In Proceedings of the 2012 Conference on Precision Electromagnetic Measurements, Washington, DC, USA, 1–6 July 2012; pp. 636–637.
22. Phaebua, K.; Lertwiriayaprapa, T.; Torrungrueng, D. Cylindrical near-field to far-field radiation pattern measurement system for a large mobile phone base station antenna. In Proceedings of the 2021 International Electrical Engineering Congress (IEECON2021), Pattaya, Thailand, 10–12 March 2021; pp. 535–538.
23. Paraskevopoulos, A.; Tsolis, A.; Vardaxoglou, J.C.; Alexandridis, A.A. Cylindrical near-field assessment of wearable antennas for body-centric communications. *IET Microw. Antennas Propag.* **2017**, *11*, 761–769. [[CrossRef](#)]
24. Bucci, O.M.; Gennarelli, C.; Savarese, C. Representation of electromagnetic fields over arbitrary surfaces by a finite and nonredundant number of samples. *IEEE Trans. Antennas Propag.* **1998**, *46*, 351–359. [[CrossRef](#)]
25. Yaccarino, R.G.; Williams, L.I.; Rahmat-Samii, Y. Linear spiral sampling for the bipolar planar antenna measurement technique. *IEEE Trans. Antennas Propag.* **1996**, *44*, 1049–1051. [[CrossRef](#)]
26. D'Agostino, F.; Ferrara, F.; Gennarelli, C.; Guerriero, R.; Migliozi, M. Laboratory tests assessing NF–FF transformation with helicoidal scanning for electrically long antennas. *Prog. Electromagn. Res.* **2009**, *PIER 98*, 375–388. [[CrossRef](#)]
27. D'Agostino, F.; Ferrara, F.; Fordham, J.A.; Gennarelli, C.; Guerriero, R.; Migliozi, M.; Riccio, G.; Rizzo, C. An effective near-field–far-field transformation technique for elongated antennas using a fast helicoidal scan. *IEEE Antennas Propag. Magaz.* **2009**, *51*, 134–141.
28. Costanzo, S.; Di Massa, G. Far-field reconstruction from phaseless near-field data on a cylindrical helix. *J. Electromagn. Waves Appl.* **2004**, *18*, 1057–1071. [[CrossRef](#)]
29. Cicchetti, R.; D'Agostino, F.; Ferrara, F.; Gennarelli, C.; Guerriero, R.; Migliozi, M. Near-field to far-field transformation techniques with spiral scanings: A comprehensive review. *Int. J. Antennas Propag.* **2014**, *2014*, 143084. [[CrossRef](#)]
30. Garcia-Fernandez, M.; Álvarez-Lopez, Y.; Heras, F.L. Unmanned aerial system for antenna measurement and diagnosis: Evaluation and testing. *IET Microw. Antennas Propag.* **2019**, *13*, 2224–2231. [[CrossRef](#)]
31. Mauermayer, R.A.M.; Kornprobst, J. A cost-effective tethered-UAV-based coherent near-field antenna measurement system. *IEEE Open J. Antennas Propag.* **2022**, *3*, 984–1002. [[CrossRef](#)]
32. Fernández, M.G.; Álvarez López, Y.; Andrés, F.L. Advances in antenna measurement and characterization using unmanned aerial vehicles. In Proceedings of the 2019 European Conference on Antennas and Propagation (EUCAP), Krakow, Poland, 31 March–5 April 2019; pp. 1–5.
33. Wittmann, R.C.; Alpert, B.K.; Francis, M.H. Near-field antenna measurements using nonideal measurement locations. *IEEE Trans. Antennas Propag.* **1998**, *46*, 716–722. [[CrossRef](#)]

34. Wittmann, R.C.; Alpert, B.K.; Francis, M.H. Near-field, spherical scanning antenna measurements with nonideal probe locations. *IEEE Trans. Antennas Propag.* **2004**, *52*, 2184–2186. [[CrossRef](#)]
35. Farouq, M.; Serhir, M.; Picard, D. Matrix method for far-field calculation using irregular near-field samples for cylindrical and spherical scanning surfaces. *Prog. Electromagn. Res.* **2015**, *63*, 35–48. [[CrossRef](#)]
36. Bevilacqua, F.; D’Agostino, F.; Ferrara, F.; Gennarelli, C.; Guerriero, R.; Migliozi, M.; Riccio, G. Pattern reconstruction from near-field data affected by 3D probe positioning errors collected via planar-wide mesh scanning. *Electronics* **2023**, *12*, 542. [[CrossRef](#)]
37. Bevilacqua, F.; D’Agostino, F.; Ferrara, F.; Gennarelli, C.; Guerriero, R.; Migliozi, M.; Riccio, G. An efficient procedure to compensate for the errors due to the probe mispositioning in a cylindrical near-field facility. *Sensors* **2024**, *24*, 1787. [[CrossRef](#)] [[PubMed](#)]
38. Joy, E.B.; Wilson, R.E. A simplified technique for probe position error compensation in planar surface near-field measurements. In Proceedings of the 1982 Antenna Measurement Techniques Association (AMTA), Las Cruces, NM, USA, 5–7 October 1982; pp. 14.1–14.10.
39. D’Agostino, F.; Ferrara, F.; Gennarelli, C.; Guerriero, R.; Migliozi, M. An iterative technique to compensate for positioning errors in the NF-FF transformation with helicoidal scanning for long antennas. *Prog. Electromagn. Res. C* **2011**, *18*, 73–86. [[CrossRef](#)]
40. D’Agostino, F.; Ferrara, F.; Gennarelli, C.; Guerriero, R.; Migliozi, M. Far-field pattern reconstruction from positioning errors affected near-field data acquired via helicoidal scanning. *J. Electromagn. Analys. Appl.* **2012**, *4*, 60–68. [[CrossRef](#)]
41. Bucci, O.M.; D’Elia, G.; Migliore, M.D. Advanced field interpolation from plane-polar samples: Experimental verification. *IEEE Trans. Antennas Propag.* **1998**, *46*, 204–210. [[CrossRef](#)]
42. Yaghjian, A.D. Approximate formulas for the far field and gain of open-ended rectangular waveguide. *IEEE Trans. Antennas Propag* **1984**, *32*, 378–384.

Disclaimer/Publisher’s Note: The statements, opinions and data contained in all publications are solely those of the individual author(s) and contributor(s) and not of MDPI and/or the editor(s). MDPI and/or the editor(s) disclaim responsibility for any injury to people or property resulting from any ideas, methods, instructions or products referred to in the content.